EARTH SCIENCES

The discovery of a conjugate system of faults in the Wharton Basin intraplate deformation zone

Satish C. Singh,[1,2]* Nugroho Hananto,[3] Yanfang Qin,[1] Frederique Leclerc,[2] Praditya Avianto,[4] Paul E. Tapponnier,[2] Helene Carton,[1†] Shengji Wei,[2] Adam B. Nugroho,[5] Wishnu A. Gemilang,[6] Kerry Sieh,[2] Sylvain Barbot[2]

The deformation at well-defined, narrow plate boundaries depends on the relative plate motion, but how the deformation takes place within a distributed plate boundary zone remains a conundrum. This was confirmed by the seismological analyses of the 2012 great Wharton Basin earthquakes [moment magnitude (M_w) 8.6], which suggested the rupture of several faults at high angles to one another. Using high-resolution bathymetry and seismic reflection data, we report the discovery of new N294°E-striking shear zones, oblique to the plate fabric. These shear zones are expressed by sets of normal faults striking at N335°E, defining the direction of the principal compressional stress in the region. Also, we have imaged left-lateral strike-slip faults along reactivated N7°E-oriented oceanic fracture zones. The shear zones and the reactivated fracture zones form a conjugate system of faults, which accommodate present-day intraplate deformation in the Wharton Basin.

INTRODUCTION

Plate boundaries are the key elements of plate tectonics. There are three types of plate boundaries: convergent, divergent, and transform or strike-slip boundaries. The deformation along these plate boundaries is controlled by the motion between the plates, evidenced by the occurrence of different types of earthquakes. For example, normal faulting earthquakes are generally produced at divergent plate boundaries, whereas dominantly thrust earthquakes occur at convergent boundaries. Therefore, the nature of deformation along plate boundaries is well understood, and the direction of maximum stress is more or less well defined. However, the deformation on plate boundaries sometimes induces stresses within a plate hundreds of kilometers away from the major plate boundaries, creating large-scale distributed deformation zones. One of the largest diffuse deformation zones lies in the equatorial Indian Ocean, extending from the Chagos-Laccadive Ridge in the west to the Investigator Ridge in the east for more than 3000 km (*1*–*7*). Near the Chagos-Laccadive Ridge, the deformation is expressed as a north-south extension, whereas in the Central Indian Ocean Basin (*4*), west of the Ninety East Ridge, the deformation takes place along east-west–trending thrust faults related to the north-south compression, resulting from the continental collision of India with Eurasia (*8*, *9*). To the east of the Ninety East Ridge in the Wharton Basin, the deformation is suggested to take place along the north-south–trending reactivated fracture zones with left-lateral strike-slip motion (*10*, *11*). This is due to both variable obliquity and rate of the subduction of the Indo-Australian composite plate beneath the Sunda plate in the Andaman-Sumatra region, creating a very large scale diffuse deformation zone in the Wharton Basin with poorly defined direction of maximum stress (*6*, *7*, *12*, *13*). The Indo-Australian composite plate comprises the Indian, Capricorn, Australian, and Macquarie component of plates and multiple diffuse plate boundaries (*2*–*5*, *7*).

The presence of active deformation in the Wharton Basin was confirmed by the occurrence of a series of strike-slip earthquakes in 2012 starting on 10 January 2012 with a moment magnitude (M_w) 7.2 earthquake, followed by the 11 April 2012 twin events of M_w 8.6 and M_w 8.2 (*14*–*20*) (Fig. 1), the largest intraplate earthquakes ever observed on Earth. More recently, an M_w 7.8 strike-slip earthquake occurred on 2 March 2016 (*21*) further south (~5°S). Although the foreshock of January 10 and the great aftershock of April 11 seem to have ruptured reactivated fracture zones (F6/F7) (*22*, *23*), the seismological and geodetic inversions for the largest event of M_w 8.6 require a complex faulting pattern with several faults, up to six, oblique to each other (*14*–*18*), requiring the existence of a new set of faults (Fig. 1 and fig. S1). However, the existing seismic and bathymetric data from the region have not shown the presence of any such faults (*22*–*26*).

The lithosphere in this part of the Indian Ocean was created at the Wharton Spreading Centre. Seafloor spreading in the Indian Ocean initiated around 133 Ma, as India separated from Australia, with a spreading rate reaching 40 mm/year at 80 My and increasing to 150 mm/year at 67 My as India started to move rapidly northward (*27*, *28*). As India started indenting Eurasia around 50 Ma, it slowed down to 50 mm/year at 45 My, and spreading ceased at 40 My when India and Australia became a single plate. The spreading ridge fabric (abyssal hill normal faults) is generally east-west, whereas the fracture zones are close to north-south. Present-day left-lateral motion along these reactivated fracture zones in the Wharton Basin is consistent with the increasing obliquity and decreasing convergence rate of the Indo-Australian plate from Java (orthogonal at 60 mm/year) in the east to Sumatra (54 mm/year) in the west, and nearly arc-parallel near the Andaman Islands (43 mm/year) (*29*, *30*), leading to the reactivation of fracture zones capable of hosting great earthquakes.

RESULTS

In May 2015, high-resolution bathymetry and seismic reflection data were acquired on board the Schmidt Ocean Institute (SOI)

[1]Equipe de Géosciences Marines, Institut de Physique du Globe de Paris (CNRS, Paris Diderot, Sorbonne Paris Cité), 1 rue Jussieu, 75238 Paris Cedex 05, France. [2]Earth Observatory of Singapore, Nanyang Technological University, N2-01A-XX, 50 Nanyang Avenue, Singapore 639798, Singapore. [3]Research Center for Geotechnology, Indonesian Institute of Sciences, Komplek LIPI Jl., Sangkuriang Bandung 40135, Indonesia. [4]Research Center for Oceanography, Indonesian Institute of Sciences, Jl Pasir Putih 1 Ancol Timur, Jakarta Utara 14430, Indonesia. [5]Technology Center for Marine Survey, Agency for the Assessment and Application of Technology, BPPT Gedung 1 Lantai 18 Jl. MH Thamrin No. 8, Jakarta Pusat 10340, Indonesia. [6]Research Institute for Coastal Resources and Vulnerability, Ministry of Marine and Fisheries, Jl. Padang-Painan km. 16, Bungus, Padang 25245, Indonesia.
*Corresponding author. Email: singh@ipgp.fr
†Adjunct Research Scientist at the Lamont-Doherty Earth Observatory, Columbia University, Palisades, NY 10964, USA.

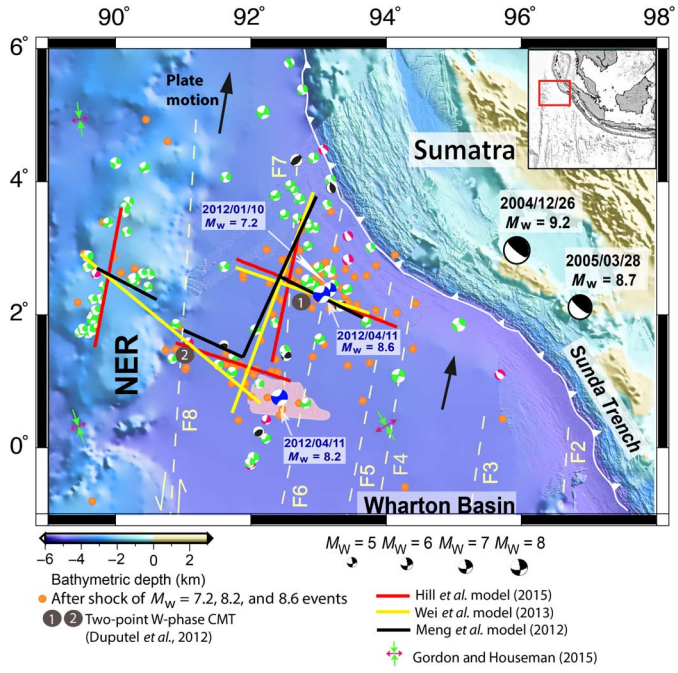

Fig. 1. The 2012 earthquake rupture zone in the Wharton Basin. The blue beach balls represent the 2012 earthquakes, and the brown circles represent the aftershocks. The green beach balls represent strike-slip earthquakes, the black beach balls represent thrust earthquakes, and the red beach balls represent normal faulting earthquakes. "1" and "2" represent two-point W-phase centroid moment tensor (CMT) solutions (*18*). NER, Ninety East Ridge. The white dashed lines indicate fracture zones F2 to F8. The red, yellow, and black lines indicate different fault models (*14*–*16*). The black arrow indicates the subduction direction. The green and purple arrows indicate the directions and the relative magnitudes of the principal deviatoric compression and tension components from Gordon and Houseman (*7*). The light pink area indicates the new bathymetry shown in Fig. 2A. The red rectangle in the inset at the right-hand upper corner shows the main study area.

research vessel (R/V) *Falkor* in the epicentral region of the 2012 M_w 8.2 earthquake and in the southern edge of the inferred rupture zone of the M_w 8.6 earthquake (see Materials and Methods). The uninterpreted bathymetry image is shown in Fig. 2A, and the interpreted images are shown in Fig. 2 (B and C).

The two most important features on this map are as follows: (i) approximately north-south–oriented reactivated fracture zones (F6 and F7) accommodating left-lateral strike-slip movement and (ii) west-northwest–striking shear zones accommodating right-lateral motion. These fracture zones were previously identified using magnetic anomalies (*28*) and seismic reflection studies (*22*, *23*). Bathymetry and seismic images show recent deformations associated with these structures. The easternmost fault of the reactivated fracture zone set, F6a, has a fresh and clear bathymetric expression on the seafloor, seems to be the most active, and strikes at N9°E (Figs. 2B and 3A) with some west-side down-dip slip component. This left-lateral fault shows en echelon fault segments and releasing step-overs, in particular a well-developed, rhomb-shaped, pull-apart basin that is 4 km long, 2.5 km wide, and 95 m deep. F6b is parallel to F6a at ~10 km further west. It consists of right-stepping, east-dipping en echelon faults that are 1 to 5 km long. The westward dip of F6a and the eastward dip of F6b, combined with the dominance of F6a, suggest that F6b might be the conjugate of the master fault F6a.

The westernmost north-south feature, fault F7b located at 25 km west of F6b, also consists of en echelon faults striking at N6°E (Fig. 2B) with some eastward dip component. The epicenter of 11 April 2012 M_w 8.2 earthquake lies on F7b. These three reactivated fracture zones (F6a, F6b, and F7b) define a ~35-km-wide zone with an average strike of N7°E (Fig. 3A), where the left-lateral motion is localized.

On both east and west sides of the region of reactivated fracture zones, we observe many N294 ±4°–trending right-lateral shear zones (Figs. 2B and 3B) spaced at 5 to 10 km. These shear zones are, on average, ~2.5 km wide and appear as a series of elongated depressions bounded by sets of en echelon normal faults. The vertical offset on the seafloor along these normal faults is on the scale of 4 to 10 m, and their strike is N335 ±3° (Fig. 3C). Several north-south–oriented channels are also present west of the fracture zones. They flow southward, across the shear zones, and their bed is deflected by the presence of depressions within the shear zones. It is interesting to note that the shear zones do not cross the F6-F7 fracture zone system: They are imaged on both sides, but not in the intervening regions. We interpret the N294°-striking right-lateral shear zones and the left-lateral N7°E-striking reactivated fracture zones as conjugate faults along which the deformation is partitioned in the Wharton Basin. The left-lateral strike-slip faults are expressed by releasing step-overs or right-stepping en echelon faults, whereas the right-lateral shear zones are expressed as a set of en echelon normal faults defining the direction of extension in the region. Consequently, the strike of the small N335° normal faults represents the direction of the maximum horizontal compressional stress in the study area (Fig. 3C).

The age of the oceanic lithosphere across these four fracture zones is 52.6 to 54.8 My in the east and 63.1 to 64.2 My in the west (Fig. 2B), and the crustal thickness is 3.5 to 4.5 km in the east and 6 km in the west (*22*, *23*), but the nature of the shear zones is similar on both sides. The strike of spreading-related normal faulting in the Wharton Basin is east-west, but the shear zones are oblique to these preexisting structures, suggesting that the shear zones are new and not reactivated spreading-related normal faults.

The sediment thickness over the normal oceanic crust, away from the fracture zones, is ~2.2 km (Figs. 4 and 5). A 200- to 300-m-thick, poorly reflective layer is imaged just above the basement, bounded at its top by what might be the pelagic/hemipelagic sediment transition, similar to observations reported further north (*22*, *25*). Turbiditic sediments (~2 km) that have likely been deposited after the collision of India with Eurasia about 40 Ma lie above this lowermost unit. These sediments belong to the Nicobar Fan, similar to the Bengal Fan sediments but east of the Ninety East Ridge, carried by the Ganges and Brahmaputra river system, channeled between the Ninety East Ridge and Sunda Trench, and spread over thousands of kilometers (*31*). If we assume a constant sedimentation rate, then the sedimentation rate would be 50 m/My, rather high for such a distal abyssal plain, but similar to that observed further north (*25*).

Seismic reflection images document the activity along faults F6 and F7 (Fig. 4), whose different strands can be traced from the seafloor down to the basement. Basement reliefs of 0.6 to 1.7 km, generally containing a basement high (ridge) and low (depression), are imaged in relation to these faults. Seismic reflection data confirm that F6a is the most active fault of the reactivated fracture zone set. In the south, fault F6a is vertical and its trace is located 2 to 3 km east of the basement high. It crosscuts the sediments like a knife

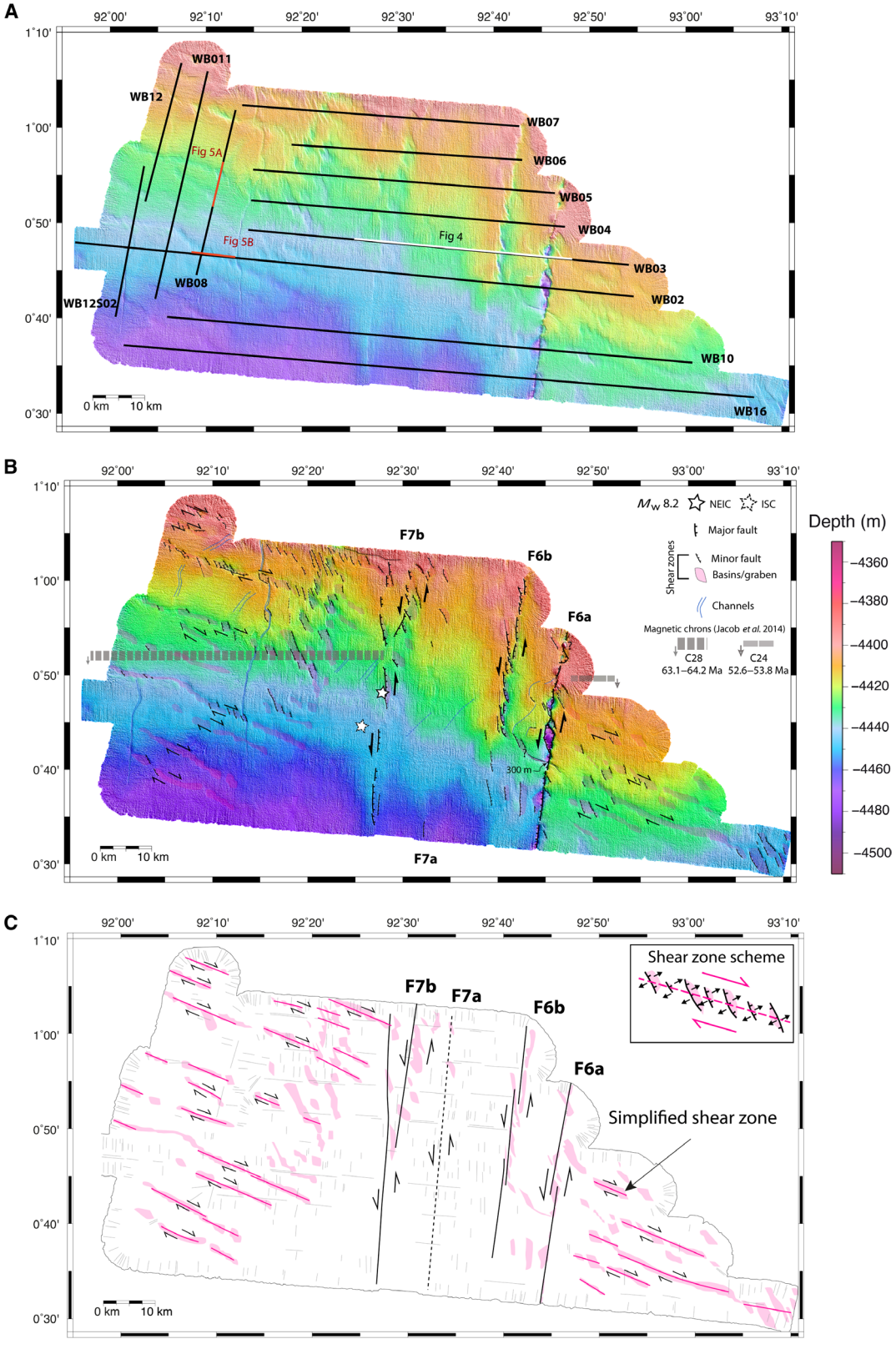

Fig. 2. New bathymetry. (**A**) Uninterpreted bathymetry. Black lines represent seismic profiles acquired. The white line shows the position of the seismic image shown in Fig. 4, and the red lines show the position of the seismic image shown in Fig. 5. (**B**) Interpreted bathymetry. F6a and F7b, reactivated fracture zones. Different symbols are defined in the right-hand upper corner. NEIC, National Earthquake Information Center; ISC, International Seismological Centre. (**C**) Simplified interpreted bathymetry showing main features. The inset shows a schematic shear zone scheme.

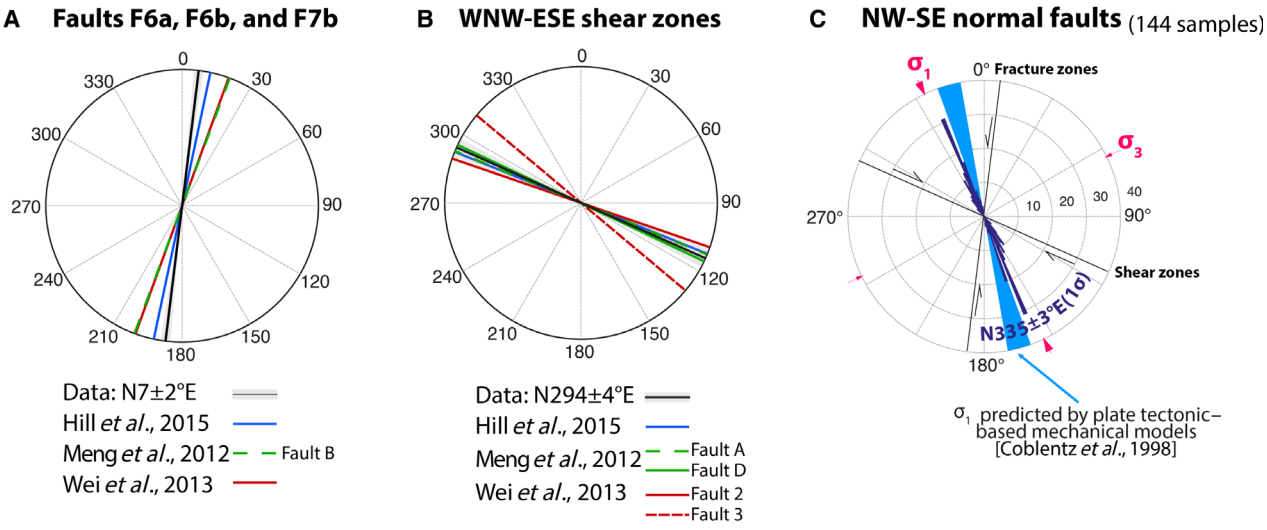

Fig. 3. Rose diagrams. The rose diagrams for the average strike of the reactivated fracture zones F6a, F6b, and F7 (**A**); the shear zones (**B**); and normal faults bounding the shear zones (blue) (**C**). Black lines indicate the two conjugate strike-slip faults. σ_1 (red) is the principal compressional stress, and σ_3 is the principal extensional stress. The light blue marks the principal compressional stress direction determined by one of the previous studies (*13*).

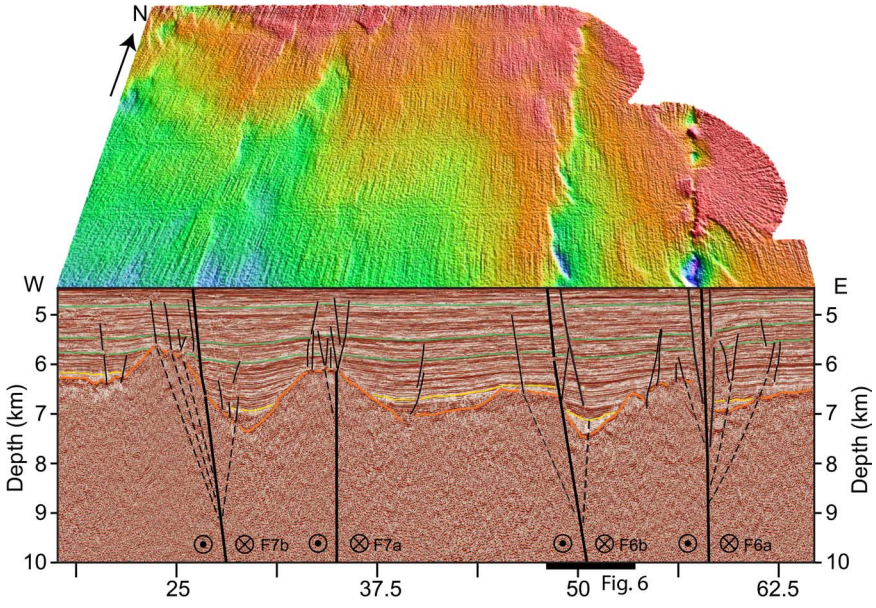

Fig. 4. Interpreted seismic reflection image across reactivated fracture zones. Seismic reflection along profile WB03 crossing through four reactivated fracture zones (F6a, F6b, F7a, and F7b). Prominent sedimentary horizons are marked in green. The yellow line marks the top of the pelagic sediments. The red curve marks the top of oceanic basement. Thick black lines, major faults; thin black lines, minor faults. Dashed thin black lines link faults imaged in the sediments with deep-rooted strike-slip faults.

(fig. S2B), possibly breaking through the oceanic crust that forms new faults (fig. S2B). Further north, sediment deformation at depth records the development of a pull-apart basin already identified from the bathymetry (fig. S2C). North of the main pull-apart basin, the fault lies close to the basement high (fig. S2D).

Fault F6b is best expressed in the northern part of the study area, consisting of eastward dipping fault segments. It is associated with a basement high flanked by a bathymetric low (fig. S3), and the fault extends at depth through this bathymetric low. Fault F7b is present along the whole north-south extent of the survey area and is associated with a prominent (1.5-km) basement ridge (fig. S4). Another basement ridge with a 1.2-km relief is imaged in seismic data 10 km east of F7b, associated with a fault strand that we call F7a (Fig. 4). F7a is less active, with little surface expression, and F7a, at depth, cuts across the basement high instead of the slope (Fig. 4).

The 294° azimuth shear zones are expressed by flower structures with a set of faults dipping inward with a dip of 65° to 70° (Fig. 5), defining the location of strike-slip faults at depth, with the innermost pair of faults joining at a depth of ~5.6 km (Fig. 5). Some of the faults can be traced down to the basement, which they seem to offset. The number of faults seems to increase below ~5.6 km due to the complex interaction between the normal faulting, the shear zone, and the faults

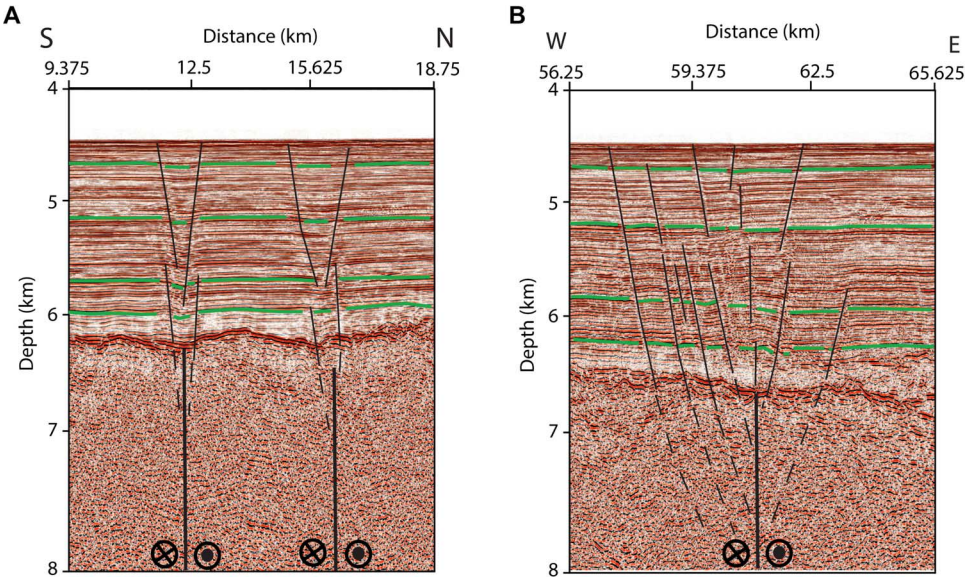

Fig. 5. Seismic reflection images of shear zones. (**A**) Interpreted seismic image across a shear zone along the north-south profile WB08. (**B**) Interpreted seismic image across a shear zone along the east-west profile WB02. Green lines represent sedimentary strata, black lines represent faults, and very thick lines represent deep faults.

at depth (Fig. 5B). These shear zones are different from the Riedel shears observed by Geersen *et al.* (*25*) further north in the outer rise area that might have been influenced by the plate bending, but some of the Riedel shears striking 330° to 360° might be genetically related to the 335°-striking normal faults that we observe in our study. Similarly, faults west of fracture zone F5 (fig. S5) have strikes between 330° and 340°, indicating that they might also have a similar origin.

Although the basement highs and lows along the traces of F6 and F7 might represent the original fracture zone morphology, the sediment deposition patterns indicate a westward flexural rotation of the basement ridges and subsidence in the adjacent lows (fig. S4). Regions of active faulting along the reactivated fracture zones are typically 3 to 4 km wide and contain several en echelon fault segments, which make it difficult to characterize the age and evolution of these faults from limited two-dimensional seismic reflection data (Fig. 4). F6b seems to contain only two major fault branches (F6b1 and F6b2), allowing us to get some idea about the evolution of fault activity over time (Fig. 6). The cumulative vertical offset across the two branches of F6b measured along profile WB03 increases with depth up to ~5.6 km, corresponding to an age of 17.5 My, and then remains constant below this depth, suggesting that the reactivation along these fracture zones started ~17.5 My, similar to that in the Central Indian Ocean (*32*), coinciding with the uplift of the Himalayas (*33*). For F6b1, we find two distinct slopes, corresponding to the age variations from 0 to 7 My and 7 to 17.5 My, which could be due to a change in either the sedimentation or the deformation rate. This transition at ~7 My corresponds to the uplift of Tibet (*32*, *33*), although there is still some debate about the timing of the uplift of Tibet (*34*). A similar pattern is observed along some of the other profiles (fig. S6).

Vertical offsets on the seafloor along the normal faults associated with the shear zones are small (4 to 10 m), but one can clearly observe growth with depth reaching up to 20 to 30 m (fig. S7), with a maximum at a depth of 5.6 km (17.5 My) (fig. S7), which coincides with the sudden increase in the number of faults below this depth (Fig. 5B), suggesting that these shear zones also initiated at the same time.

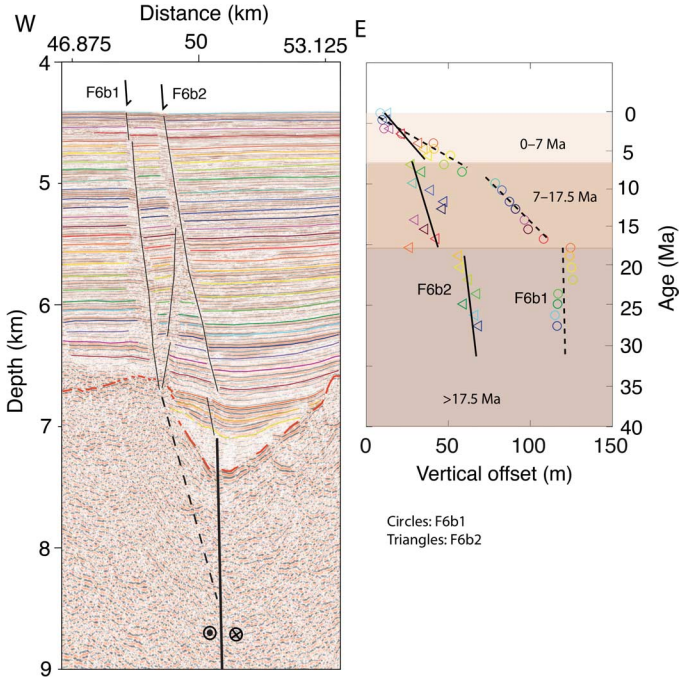

Fig. 6. The vertical cumulative offset on F6b. Interpreted seismic image across F6b along profile WB03 (left) and the cumulative offset as a function of depth across two branches of F6b (F6b1 and F6b2) and as a function of age up to 40 My. F6b1 and F6b2 are two branches of reactivated fracture zone F6b (right). Horizontal color lines indicate horizons used in the right panel. The thin black lines indicate interpreted faults in the sediments, and the thick solid black line indicates the possible position of reactivated fracture zone at depth.

DISCUSSION

The conjugate nature of deformation along the reactivated fracture zones (F6/F7) and the N294°-striking shear zones might be able to reconcile the discrepancy between the rupture models of the 2012

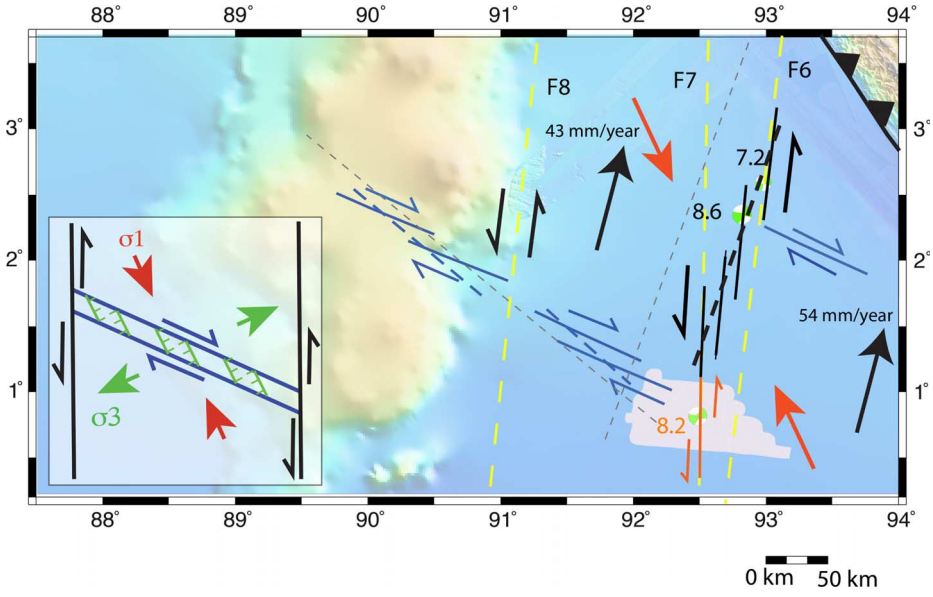

Fig. 7. En echelon faulting and the deformation in the Wharton Basin. Schematic diagram showing the en echelon rupture during the 2012 M_w 8.6 earthquake. The black solid lines indicate the reactivated fracture zones in an en echelon form (F6a, F6b, F7a, and F7b) along fracture zones (F6 and F7 in yellow). The blue lines indicate en echelon rupture along the shear zones. The M_w 8.2 ruptured fracture zone F7b is marked in orange. The light purple area is shown in Fig. 2. The long black arrows and numbers indicate the direction of subduction and approximate convergence rates (*29*). The long red arrows indicate the direction of the principal compressional stress determined from our study. The dashed black and blue lines indicate average strike direction of faults during the 2012 M_w 8.6 rupture. Thin dashed gray lines indicate faults F2 and F3 from Wei *et al.* (*16*). The inset shows the conjugate faulting along the reactivated fracture zones (black) and shear zones (blue) and the direction of principal compressional (σ_1) (red arrow) and extensional (σ_3) (green) stresses.

M_w 8.6 earthquake and the seafloor observations. The total width of the reactivated fracture zone regions in our study area is 35 km, and the one north of the M_w 8.6 epicenter is ~42 km (*23*). Also in that area, we observe four faults along reactivated fracture zones with strike varying from 0° to N6°E, suggesting that fracture zones F6 and F7 continue all the way to the subduction front. Furthermore, there is also some evidence of N335°-striking normal faulting in the north on the outer rise at 60 km from the subduction front (fig. S5), suggesting that the deformation along this azimuth is common in the Wharton Basin. The M_w 8.6 earthquake likely ruptured several distinct fault segments, among which at least one was along the north-northeast–south-southwest segment in the vicinity of F6/F7 (Fig. 7). We suggest that the M_w 8.6 earthquake ruptured F6a to F7b in an en echelon form, south stepping and breaking segments of ~75- to 100-km length each (Fig. 7). Because the inversion of seismological and geodetic data record can only use long wavelength signals hundreds and thousands of kilometers away from the rupture location, these data cannot resolve the slip along each segment separately but instead provide an average solution (Fig. 7 and fig. S1). Similarly, the closely spaced N294°-striking shear zone might have ruptured in an en echelon form, westward stepping and breaking in smaller segments. The en echelon rupture along these faults can explain the discrepancies between the seafloor observation and the different rupture models (Fig. 7).

Finite fault models of the 2012 earthquakes suggest that these earthquakes ruptured down to the base of the lithosphere at a depth of 40 to 50 km (*14*, *16*). Qin and Singh (*26*) have imaged faults down to a depth of 45 km in this area. Because the oceanic lithosphere in this area was formed at a fast spreading environment, the original fracture zone–related faults should have been shallow (~6 km) (*35*), overlying a thin lithosphere when they formed, indicating that the deep lithospheric faulting in the Wharton Basin is related to the recent intraplate deformation.

The direction of principal compression in the Wharton Basin is poorly constrained, varying from 315° to 350° (*7*, *12*, *13*). In our survey area, the strike of the reactivated fracture zones is ~N7 ±2°E, whereas the strike of the shear zones is N294 ±4°E. Hence, the angle between the two principal directions of motion is ~75 ±4.5°, slightly larger than the 60° expected for conjugate shear faults. The strike of the normal faults bounding the shear zones is N335 ±3°E, that is, ~34° from the reactivated fracture zones and 41° from the average orientation of the shear zones, nearly half (37.5 ±4°) of the angle between the two conjugate faults, suggesting that the 335° azimuth is the principal stress direction in the Wharton Basin with an average static friction of 0.26 along conjugate faults (*36*). However, it could be as small as 0.14 along the reactivated fracture zones and up to ~0.40 along the shear zones. The weakness of the reactivated fracture zones may be due to the accumulation of large co-seismic slip with strong dynamic weakening (*37*). Experimental investigation of frictional resistance at high slip rates indicates that thermally activated processes may largely reduce fault friction (*38*–*40*). This would be possible if the fracture zones repeatedly hosted great earthquakes such as the 2012 sequence. Furthermore, these fracture zones with a large age and crustal thickness contrast (F6/F7 and F8) can act as a boundary for the differential plate motion, enhancing the strain accumulation across them, as was suggested by the Coulomb stress change estimated after the 2004 great megathrust earthquake (*41*). These effects, combined with the 335° azimuth principal compressive stress, would strongly encourage rupture along the north-south fracture zones, acting as the main zone of deformation in the Wharton Basin and possibly leading to the creation of a new plate boundary in the Indian Ocean. The presence of strike-slip earthquakes along the fracture zone F6/F7 over a length

of 1000 km (*23*) suggests that these fracture zones could be a nascent plate boundary.

MATERIALS AND METHODS

High-resolution bathymetry and seismic reflection data were acquired on board the SOI R/V *Falkor*. The R/V *Falkor* was equipped with a multibeam swath bathymetry system with a dominant frequency of 27 kHz (EM 321), leading to a very high resolution image of the seafloor. At a water depth of 4500 m in the study area, the vertical resolution is 3 to 4 m and the lateral resolution is 25 m, providing an unprecedented image of the seafloor. In 1 week, we covered an area of 750 km^2 that includes about a 75-km segment of F6/F7 fracture zones and about 50 km of oceanic crust on either side of these fracture zones (Fig. 2A). Coincidently, high-resolution seismic reflection data were acquired at a line spacing of 6 km (Fig. 2A). A two-gun cluster, with a total volume of 8.19 liters, fired at a 25-m interval, was used as the source. The guns were deployed at a water depth of 3 m to generate energy up to 200 Hz. A streamer, containing 96 channels at a group interval of 12.5 m, deployed at a depth of 4.5 m, recorded the seismic energy. The seismic data were processed using conventional processing steps, including swell noise removal, binning, trace editing, velocity analysis, stacking, and post-stack time migration (*42*). The data were converted to depth using seismic velocity information that was obtained further north (*43*). After processing, the lateral trace spacing is 6.25 m, and the vertical resolution is 4 m for a dominant frequency of 100 Hz.

SUPPLEMENTARY MATERIALS

Supplementary material for this article is available at http://advances.sciencemag.org/cgi/content/full/3/1/e1601689/DC1

fig. S1. Different models of the 2012 M_w 8.6 earthquake.
fig. S2. Seismic reflection images of F6a.
fig. S3. Seismic reflection images of F6b.
fig. S4. Seismic reflection images of F7b.
fig. S5. Bathymetry in the outer rise region.
fig. S6. Fault offset with age.
fig. S7. Blow-up seismic image of shear zone.

REFERENCES AND NOTES

1. J. K. Weissel, R. N. Anderson, C. A. Geller, Deformation of the Indo-Australian plate. *Nature* **287**, 284–291 (1980).
2. D. A. Wiens, C. DeMets, R. G. Gordon, S. Stein, D. Argus, J. F. Engeln, P. Lundgren, D. Quible, C. Stein, S. Weinsten, D. F. Woods, A diffuse plate boundary model of Indian Ocean tectonics. *Geophys. Res. Lett.* **12**, 429–432 (1985).
3. J.-Y. Royer, R. G. Gordon, The motion and boundary between the Capricorn and Australian plates. *Science* **227**, 1268–1274 (1997).
4. R. G. Gordon, C. DeMets, J.-Y. Royer, Evidence for long-term diffuse deformation of the lithosphere of the equatorial Indian Ocean. *Nature* **395**, 370–374 (1998).
5. C. DeMets, R. G. Gordon, D. F. Argus, Geological current plate motions. *Geophys. J. Int.* **181**, 1–80 (2010).
6. M. Delescluse, N. Chamot-Rooke, Instantaneous deformation and kinematics of the India-Australia plate. *Geophys. J. Int.* **168**, 818–842 (2007).
7. R. G. Gordon, G. A. Houseman, Deformation of Indian Ocean lithosphere: Evidence for a highly nonlinear rheological law. *J. Geophys. Res.* **121**, 4434–4449 (2015).
8. J. M. Bull, R. A. Scrutton, Fault reactivation in the central Indian Ocean and the rheology of oceanic lithosphere. *Nature* **344**, 855–858 (1990).
9. N. Chamot-Rooke, F. Jestin, B. de Voogd; Phèdre Working Group, Intraplate shortening in the central Indian Ocean determined from a 2100-km-long north–south deep seismic reflection profile. *Geology* **21**, 1043–1046 (1993).
10. C. Deplus, M. Diament, H. Hebert, G. Bertrand, S. Dominguez, J. Dubois, J. Malod, P. Patriat, B. Pontoise, J.-J. Sibilla, Direct evidence of active deformation in the eastern Indian oceanic plate. *Geology* **26**, 131–134 (1998).
11. C. Deplus, Indian Ocean actively deforms. *Science* **292**, 1850–1851 (2001).
12. S. Cloetingh, R. Wortel, Stress in the Indo-Australian plate. *Tectonophysics* **132**, 49–67 (1986).
13. D. D. Coblentz, S. Zhou, R. R. Hillis, R. M. Richardson, M. Sandiford, Topography, boundary forces, and the Indo-Australian intraplate stress field. *J. Geophys. Res. Solid Earth* **103**, 919–931 (2015).
14. H. Yue, T. Lay, K. D. Koper, En *échelon* and orthogonal fault ruptures of the 11 April 2012 great intraplate earthquakes. *Nature* **490**, 245–249 (2012).
15. L. Meng, J.-P. Ampuero, J. Stock, Z. Duputel, Y. Luo, V. C. Tsai, Earthquake in a maze: Compressional rupture branching during the 2012 M_w 8.6 Sumatra earthquake. *Science* **337**, 724–726 (2012).
16. S. Wei, D. Helmberger, J.-P. Avouac, Modeling the 2012 Wharton Basin earthquake off Sumatra; complete lithospheric failure. *J. Geophys. Res.* **118**, 3592–3609 (2013).
17. E. M. Hill, H. Yue, S. Barbot, T. Lay, P. Tapponnier, I. Hermawan, J. Hubbard, P. Banerjee, L. Feng, D. Natawidjaja, K. Sieh, The 2012 M_w 8.6 Wharton Basin sequence: A cascade of earthquakes generated by near orthogonal, young, oceanic mantle faults. *J. Geophys. Res.* **120**, 3723–3747 (2015).
18. Z. Duputel, H. Kanamori, V. C. Tsai, L. Rivera, L. Meng, J.-P. Ampuero, J. M. Stock, The 2012 Sumatra great earthquake sequence. *Earth Planet. Sci. Lett.* **351–352**, 247–257 (2012).
19. C. Satriano, E. Kiraly, P. Bernard, J.-P. Vilotte, The 2012 Mw 8.6 Sumatra earthquake: Evidence of westward sequential seismic ruptures associated to the reactivation of a N-S ocean fabric. *Geophys. Res. Lett.* **39**, L15302 (2012).
20. M. Ishii, E. Kiser, E. L. Geist, M_w 8.6 Sumatran earthquake of 11 April 2012: Rare seaward expression of oblique subduction. *Geology* **41**, 319–322 (2013).
21. T. Lay, L. Ye, C. J. Ammon, A. Dunham, K. D. Koper, The 2 March 2016 Wharton Basin M_w 7.8 earthquake: High stress drop north-south strike-slip rupture in the diffuse oceanic deformation zone between the Indian and Australian Plates. *Geophys. Res. Lett.* **43**, 7937–7945 (2016).
22. S. C. Singh, H. Carton, A. S. Chauhan, S. Androvandi, A. Davaille, J. Dyment, M. Cannat, N. D. Hananto, Extremely thin crust in the Indian Ocean possibly resulting from Plume–Ridge interaction. *Geophys. J. Int.* **184**, 29–42 (2011).
23. H. Carton, S. C. Singh, N. D. Hananto, J. Martin, Y. S. Djajadihardja, Udrekh, D. Franke, C. Gaedicke, Deep seismic reflection images of the Wharton Basin oceanic crust and uppermost mantle offshore northern Sumatra: Relation with active and past deformation. *J. Geophys. Res.* **119**, 32–51 (2014).
24. D. Graindorge, F. Klingelhoefer, J.-C. Sibuet, L. McNeill, T. J. Henstock, S. Dean, M.-A. Gutscher, J. X. Dessa, H. Permana, S. C. Singh, H. Leau, N. White, H. Carton, J. A. Malod, C. Rangin, K. G. Aryawan, A. Chauhan, D. R. Galih, C. J. Greenwood, A. Laesanpura, J. Prihantono, G. Royle, U. Shankar, Impact of lower plate structure on upper plate deformation at the NW Sumatran convergent margin from seafloor morphology. *Earth Planet. Sci. Lett.* **275**, 201–210 (2008).
25. J. Geersen, J. M. Bull, L. C. McNeill, T. J. Henstock, G. Gaedicke, N. Chamot-Rooke, M. Delescluse, Pervasive deformation of an oceanic plate and relationship to large >M_w 8 intraplate earthquakes: The northern Wharton Basin, India Ocean. *Geology* **43**, 359–362 (2015).
26. Y. Qin, S. C. Singh, Seismic evidence of a two-layer lithospheric deformation in the Indian Ocean. *Nat. Commun.* **6**, 8298 (2015).
27. C. S. Liu, J. R. Curray, J. M. McDonald, New constraints on the tectonic evolution of the eastern Indian Ocean. *Earth Planet. Sci. Lett.* **65**, 331–342 (1983).
28. J. Jacob, J. Dyment, V. Yatheesh, Revisiting the structure, age, and evolution of the Wharton Basin to better understand subduction under Indonesia. *J. Geophys. Res.* **119**, 169–190 (2014).
29. R. McCaffrey, P. C. Zwick, Y. Bock, L. Prawirodirdjo, J. F. Genrich, C. W. Stevens, S. S. O. Puntodewo, C. Subarya, Strain partitioning during oblique plate convergence in northern Sumatra: Geodetic and seismological constraints and numerical modeling. *J. Geophys. Res.* **105**, 28363–28376 (2000).
30. T. J. Fitch, Plate convergence, transcurrent faults, and internal deformation adjacent to Southeast Asia and the western Pacific. *J. Geophys. Res.* **77**, 4432–4460 (1972).
31. F. A. Bowles, W. F. Ruddiman, W. H. Jahn, Acoustic stratigraphy, structure, and depositional history of the Nicobar Fan, eastern Indian Ocean. *Mar. Geol.* **26**, 269–288 (1978).
32. J. R. Cochran, Himalayan uplift, sea level, and the record of Bengal Fan sedimentation at the ODP Leg 116 sites. *Proc. Ocean Drill. Program Sci. Results* **116**, 397–414 (1990).
33. K. S. Krishna, J. M. Bull, R. A. Scrutton, Early (pre–8 Ma) fault activity and temporal strain accumulation in the central Indian Ocean. *Geology* **37**, 227–230 (2009).
34. P. Molnar, W. R. Boos, D. S. Battisti, Orographic controls of climates and paleoclimates of Asia: Thermal and mechanical roles of Tibetan Plateau. *Ann. Rev. Earth Planet. Sci.* **38**, 77–102 (2010).
35. J. J. McGuire, M. S. Boettcher, T. H. Jordan, Foreshock sequences and short-term earthquake predictability on East Pacific Rise transform faults. *Nature* **434**, 457–461 (2005).
36. D. L. Turcotte, G. Schubert, *Geodynamics* (Cambridge Univ. Press, 1982).

37. H. Noda, E. M. Dunham, J. R. Rice, Earthquake ruptures with thermal weakening and the operation of major faults at low overall stress levels. *J. Geophys. Res.* **114**, B07302 (2009).
38. G. Di Toro, T. Hirose, S. Nielsen, G. Pennacchioni, T. Shimamoto, Natural and experimental evidence of melt lubrication of faults during earthquakes. *Science* **311**, 647–649 (2006).
39. G. Di Toro, D. L. Goldsby, T. E. Tullis, Friction falls towards zero in quartz rock as slip velocity approaches seismic rates. *Nature* **427**, 436–439 (2004).
40. C. A. J. Wibberley, T. Shimamoto, Earthquake slip weakening and asperities explained by thermal pressurization. *Nature* **436**, 689–692 (2005).
41. M. Delescluse, N. Chamot-Rooke, R. Cattin, L. Fleitout, O. Trubienko, C. Vigny, April 2012 intra-oceanic seismicity off Sumatra boosted by the Banda-Aceh megathrust. *Nature* **490**, 240–244 (2012).
42. S. C. Singh, H. Carton, P. Tapponnier, N. D. Hananto, A. P. S. Chauhan, D. Hartoyo, M. Bayly, S. Moeljopronoto, T. Bunting, P. Christie, H. Lubis, J. Martin, Seismic evidence for broken oceanic crust in the 2004 Sumatra earthquake epicentral region. *Nat. Geosci.* **1**, 771–2781 (2008).
43. Y. Qin, "Nature of subducting plate and its role on megathrust offshore Sumatra by using advanced analysis technique of long streamer data," thesis, Institut de Physique du Globe de Paris, France (2015).

Acknowledgments: The data were acquired on board the SOI R/V *Falkor* during the MegaTera experiment, which is an international project between the Earth Observatory of Singapore, the Indonesian Institute of Sciences, SOI, and Institut de Physique du Globe de Paris. We thank the captain and the team of R/V *Falkor* for their help and support during the experiment. Constructive reviews of R. Burgmann and J. Geersen were extremely useful. G. Houseman provided the stress data shown in Fig. 1, and the seismologist colleagues provided their fault models shown in Fig. 1 and fig. S1. These are Institut de Physique du Globe de Paris publication number 3793 and Earth Observatory of Singapore publication number 136. **Funding:** S.B. and P.E.T. were supported by the National Research Foundation of Singapore under the National Research Foundation Fellowship scheme (National Research Fellow Awards No. NRF-NRFF2013-04) and by the Earth Observatory of Singapore, the National Research Foundation, and the Singapore Ministry of Education under the Research Centres of Excellence initiative. The SOI provided the R/V *Falkor* for the experiment, and the EOS funded the renting of the seismic equipment. **Author contributions:** S.C.S. designed the experiment, led the data collection, supervised the processing and the project, and wrote the paper. K.H. was the principal investigator of the project. S.B. contributed in writing of the paper. N.H. co-led the experiment. Y.Q. processed the seismic reflection data and participated in writing the paper. P.A. led the processing of bathymetry data. F.L. participated in the interpretation of bathymetry and seismic reflection data along with P.E.T. and contributed in the writing of the paper; H.C., S.W., A.B.N., and W.A.G. participated in acquiring the data. **Competing interests:** The authors declare that they have no competing interests. **Data and materials availability:** The raw data are available at http://www.marine-geo.org/tools/new_search/index.php?&output_info_all=on&entry_id=FK150523, entitled "Processed ship-based GSF-Format Bathymetric Sonar Data (EM302) from the Sumatra-Andaman Subduction Zone acquired during Falkor expedition FK150523 (2015)," Integrated Earth Data Applications (IEDA). doi: dx.doi.org/10.1594/IEDA/322349. Processed data can be obtained upon request. All data needed to evaluate the conclusions in the paper are present in the paper and/or the Supplementary Materials. Additional data related to this paper may be requested from the authors.

Submitted 21 July 2016
Accepted 28 November 2016
Published 4 January 2017
10.1126/sciadv.1601689

Citation: S. C. Singh, N. Hananto, Y. Qin, F. Leclerc, P. Avianto, P. E. Tapponnier, H. Carton, S. Wei, A. B. Nugroho, W. A. Gemilang, K. Sieh, S. Barbot, The discovery of a conjugate system of faults in the Wharton Basin intraplate deformation zone. *Sci. Adv.* **3**, e1601689 (2017).

ScienceAdvances
AAAS

The discovery of a conjugate system of faults in the Wharton Basin intraplate deformation zone

Satish C. Singh, Nugroho Hananto, Yanfang Qin, Frederique Leclerc, Praditya Avianto, Paul E. Tapponnier, Helene Carton, Shengji Wei, Adam B. Nugroho, Wishnu A. Gemilang, Kerry Sieh and Sylvain Barbot (January 4, 2017)

Sci Adv 2017, 3:.
doi: 10.1126/sciadv.1601689